

# A Study on the Heat Effect and Kinetics During Magnesiothermic Reduction of Porous SiO<sub>2</sub>

**Boxia Zhang**

Northeastern University

**Fei wang**

Northeastern University

**Jianshe Chen**

Northeastern University

**Binchuan Li**

Northeastern University

**Kuiren Liu**

Northeastern University

**Qing Han** (✉ [hanq@smm.neu.edu.cn](mailto:hanq@smm.neu.edu.cn))

Northeastern University

---

## Research Article

**Keywords:** Si nanocrystalline, heat effect, magnesiothermic reduction kinetics, phase composition

**Posted Date:** August 26th, 2021

**DOI:** <https://doi.org/10.21203/rs.3.rs-838158/v1>

**License:**   This work is licensed under a Creative Commons Attribution 4.0 International License.

[Read Full License](#)

---

# Abstract

Magnesiothermic reduction reaction (MRR) is an effective method to synthesis Si nanoparticles. In this paper, the heat effect and MRR kinetics were investigated by real-time temperature monitoring and analyzing the DSC curve of the MRR. It was found that the MRR onset temperature is about 465 °C, and the system temperature rose sharply at 535 °C. After the disappearance of the magnesium phase, the system temperature remained consistent with the set value. The exothermic peak lags and the spike decreases when adding NaCl into the system. The MRR was chemical reaction control, corresponding with the apparent activation energy was 193.456 kJ·mol<sup>-1</sup> (without NaCl) and 191.434 kJ·mol<sup>-1</sup> (with NaCl) in the temperature interval 465 °C –700 °C, respectively. NaCl affects the reaction mechanism by lowering the temperature of the system. Our work successfully prepared the spherical Si nanoparticles, which average grain size increased from 25 nm to 40 nm with the extended reaction duration. The conversion rate of porous SiO<sub>2</sub> precursor was as high as 92%.

## 1 Introduction

As for the lithium-ion battery negative electrode materials, the graphite has approached the theoretical specific capacity (372 mAh·g<sup>-1</sup>) and cannot be an excellent match for future high energy density power batteries. Amongst the next-generation negative electrode materials, Si has received significant attention due to its high theoretical specific capacity (3579 mAh·g<sup>-1</sup> for Li<sub>15</sub>Si<sub>4</sub>) [1 – 3]. Unfortunately, the Si electrode suffers from drastic volume change (> 300%) during the charge-discharge cycle, which leads to rapid capacity loss and poor cycling performance [4 – 6]. At present, the regulation of its microstructure remains a viable candidate for relieving volume expansion in order to improve cycle life [7], e.g., nanostructured Si (nanoparticles [8], nanotubes [9 – 11], nanowires [12], and nanoporous [13 – 15]), and shell covering structures of Si-based materials (Si@C [16 – 18], Si@Cu [19], and Si@void@C [20]). In addition, nanostructured Si also is an attractive material for photovoltaics [21], photocatalysis [22], and thermoelectrics [23]. However, it remains a challenge to produce nanostructured Si at a high yield with a low cost.

In 2007, the magnesiothermic reduction reaction was firstly used to fabricate microporous Si replicas from three-dimensional SiO<sub>2</sub> micro-assemblies, which was considered one of the most promising methods to fabricate Si nanoparticles [24]. Other Si-based materials were also synthesized via the MRR [25 – 27], demonstrating a high specific capacity and excellent rate capability. It was found that the additional free spaces were why abundant mesoporous structures could effectively reduce the volume expansion of Si particles. Furthermore, Liu et al. proposed that a single Si nanoparticle (less than 150 nm), i.e., nano effect, could also alleviate the bulk expansion of the Si [28].

Among the numerous paper reported to date, the MRR was a violent exothermic reaction, which caused a large quantity of heat released and accumulated in the system. The heat effect resulted in the local temperature of the system reaching 1941°C, which significantly affected the structure of the reactant and product [29]. Shi et al. prepared the product Si nanoparticles by alleviating the massive local heat via

reducing the ramp rate [30]. Si nanoparticles also were successfully fabricated by Meekins et al., directly adding the heat scavenger NaCl into reactants of the MRR [31]. Yang et al. concluded that the quantity of the gasified magnesium decreased as their particle sizes exceed 80  $\mu\text{m}$ , avoiding sintering the solid reactant or product [32]. Another way to mitigate heat accumulation was to improve the reaction apparatus by placing Mg and  $\text{SiO}_2$  separately [33]. The above strategies have alleviated the adverse impact caused by the heat effect and have synthesized Si-based materials with excellent electrochemical properties. Nevertheless, it is still noted that the existing studies remain unclear in terms of the role of heat effect on the phase composition and the reaction kinetics of the MRR.

This work revealed the actual temperature change process within the MRR system by real-time temperature monitoring. It also determined the influence of system heat effect on the phase composition and the kinetics of the MRR process. Si nanoparticles with  $D_{(0.5)}$  of 25 nm were successfully prepared.  $D_{(0.5)}$  is the average grain size, which increased to 40 nm with the reaction duration increases, and the conversion rate of  $\text{SiO}_2$  to Si reached 92%. It is theoretical guidance for the efficient production of Si nanoparticles via the MRR.

## 2 Experimental

### 2.1 Si nanoparticles preparation

The amorphous  $\text{SiO}_2$  particles with a diameter of about 20  $\mu\text{m}$  used in this study are an aggregate formed by the non-compactly interconnected  $\text{SiO}_2$  nanoparticles ( $D_{(0.5)} = 25 \text{ nm}$ ). Firstly, The uniformly mixed amorphous  $\text{SiO}_2$  (2 g, 99.5% purity, Ningbo Jinlei Nanomaterials Technology Co., Ltd.) and Mg powder (1.6 g, 99.5% purity, China National Pharmaceutical Group Chemical Reagent Co., Ltd.) were sealed into a stainless steel container (20 mL) then transferred to a horizontal tube furnace under an argon atmosphere. A K-type high-temperature thermocouple connected to a data acquisition unit (Agilent 34970A) was inserted inside the reactant to measure the real-time temperature of the MRR. Determine when to turn off heating power based on the real-time temperature of the system. Then ramped up to a predetermined temperature with a ramp rate of  $5^\circ\text{C}\cdot\text{min}^{-1}$ . Noteworthy, we turned off heating power at the real-time temperature reached the highest point recorded by the data collector (denoted as 0 h) and heated at  $650^\circ\text{C}$  for 2 h, 4 h, and 8 h. The comparison experiment was repeated the above experimental steps after adding NaCl into the systems ( $\text{NaCl} : \text{SiO}_2 = 5:1$  in mole).

When the mixture was cooled naturally to room temperature, the obtained brown products were immersed in ethylene glycol solution, stirred magnetically for 30 minutes to remove heat scavenger NaCl. The samples were then immersed in  $2 \text{ mol}\cdot\text{L}^{-1}$  HCl solution for 12 h to remove the newly formed  $\text{MgO}$ ,  $\text{Mg}_2\text{Si}$ , and  $\text{Mg}_2\text{SiO}_4$ . After being immersed in  $1 \text{ mol}\cdot\text{L}^{-1}$  HF solution for 10 minutes to ensure the removal of unreacted or newly formed  $\text{SiO}_2$ , the Si nanoparticle aggregate was obtained. Finally, the aggregate was immersed in ethanol and ultrasonically dispersed for 30 minutes to get more uniformly distributed Si

nanoparticles. We also calculated the crystallite sizes of Si nanoparticles with Scherrer analysis. The formula is as follows:

$$L_{hkl} = \frac{K\lambda}{\beta \cos \theta}$$

1

Where,  $L_{hkl}$  is microcrystals size in the direction perpendicular to the (hkl) crystal plane;  $\lambda$  is X-ray wavelength;  $\theta$  is Bragg angle;  $\beta$  is peak width (maximum full width at half or integral width);  $K$  is Scherrer factor. Subcrystals are essentially absent in the grains of nanomaterials. Therefore,  $L_{hkl}$  can be considered as the grain size of nanoparticles.

## 2.2 Material characterization

Thermogravimetric (TG) and differential scanning calorimetry (DSC) analysis was conducted from 20°C to 800°C at a ramp rate of 5°C·min<sup>-1</sup> in argon on a TGA - DSC instrument (SDTQ 600). The X-ray diffraction (XRD) patterns were obtained using a powder diffractometer (D 8 Advance) with Cu K $\alpha$  radiation ( $\lambda = 0.1542$  nm) at 40 kV and 30 mA. The morphologies of the materials were observed by scanning electron microscopy (SEM) using a field-emission scanning electron microscope (Quanta 250 FEG) in conjunction with energy dispersive spectrometry (EDS). The microstructure of the samples was characterized by transmission electron microscopy (TEM) at an acceleration voltage of 200 kV (G 20).

## 3 Results And Discussion

The TG - DSC curves of the reaction between the Mg and SiO<sub>2</sub> mixture were displayed in Fig. 1(a). The exothermic peak occurs around 465°C, the slope of the curve at the initial stage of the reaction (465°C - 535°C) is smaller than system temperature reaches 535°C. And the highest temperature was recorded at 575°C. This means that the reaction slowly occurs at the initial stage (465°C - 535°C), the Mg pressure increases with the temperature rise. Thus the reaction is drastic once the Mg vapor pressure is sufficient to diffuse into the SiO<sub>2</sub> particles ( at 535°C). The TG curve in Fig. 1(a) indicates that the mass does not change during the reaction. Figure 1(b) shows the real-time temperature profile of the Mg reduction SiO<sub>2</sub> obtained by turn-off heating power when the system temperature reaches the exothermic spike, i.e. when the real-time temperature of the system reaches 1270°C. It observes that the temperature slowly rises as time passes, until the 86 minutes, i.e., system temperature at 465°C, the profile suddenly over set temperature and appear exothermic peak. And the profile rapidly increases from 535°C to 1270°C in 20 seconds. It suggests that the MRR releases a large amount of heat, causing the rapid rise of the actual temperature around 535°C. The mass of the reactant (~ 20 g) much larger than the DSC experimental amount (~ 5 mg) is why the highest temperature of the real-time temperature profile is higher than 575°C. The heat conduction and radiation do not effectively dissipate the large quantity of heat released from the MRR in this condition.

To alleviate the local heat accumulation of the MRR process, the heat scavenger, i.e., NaCl, was mixed into the reactants. Table 1 summarizes the adiabatic temperature of the system calculated by HSC 6.0 (Thermochemical analysis software). It clarifies the adiabatic temperature of the MRR process reaches 2325°C, and the added NaCl could reduce the heat accumulation of the MRR exothermic process effectively, shown in systems 2 – 4. Brindley et al. [34] proposed that the formation temperature of Mg<sub>2</sub>SiO<sub>4</sub> is 1100 – 1400°C, described by solid-state Eq. (5) of Table 2. Thus, adding NaCl into the reactant proportionally (NaCl : SiO<sub>2</sub> = 5 : 1 in mole) to control system temperature and avoid byproduct Mg<sub>2</sub>SiO<sub>4</sub>. In comparison, the adiabatic temperature of the system is lower when Mg<sub>2</sub>Si reacts with SiO<sub>2</sub>, as shown in system 5 of Table 1.

Table 1  
The adiabatic temperature at different NaCl addition amounts in the Mg and SiO<sub>2</sub> mixture (systems 1 – 4); Mg<sub>2</sub>Si and SiO<sub>2</sub> mixture (system 5)

Systems	SiO <sub>2</sub> / mol	Mg / mol	Mg <sub>2</sub> Si / mol	NaCl / mol	Adiabatic temperature / °C
1	1	2	0	0	2325
2	1	2	0	1	1810
3	1	2	0	3	1332
4	1	2	0	5	1017
5	1	0	1	5	812

After adding NaCl to the reactants, the TG – DSC curves of the reaction are displayed in Fig. 2(a). The exothermic peak occurs around 475°C, and the highest temperature is recorded at 533°C. It indicates that the MRR with NaCl onset temperature is about 475°C and much more violent when the system temperature reaches 533°C. Compared with the exothermic peaks in Fig. 1(a), it can be seen that the exothermic peaks lags and the highest temperature decrease. The melting of NaCl causes the sharp heat absorption peak of the DSC curve around 803°C. The TG curve in Fig. 2(a) also indicates that the mass does not change during the reaction. Figure 2(b) shows the real-time temperature profile of the Mg reduction SiO<sub>2</sub> obtained by turn-off heating power when the system temperature reaches the exothermic spike (792°C). As shown in Fig. 2(b), the exothermic peak appears when the system temperature reaches 535°C, with a temperature spike of 792°C. It is clear that adding NaCl can effectively prevent heat accumulation inside the system during the pre-reaction period (475°C – 535°C). What's more, NaCl can destroy the heat accumulation and reduces the temperature (highest temperature from 1270°C decrease to 792°C), but when the MRR is strong, NaCl cannot fully absorb the heat released near 535°C. The NaCl limits the reaction temperature rise over the NaCl melting point. Indeed, the heat released will be used to melt NaCl rather than products.

The temperature profiles in the reactor with different reaction durations (2 h, 4 h, and 8 h) at 650°C are shown in Fig. 3. There are two stages in the MRR actual temperature change process after the system temperature rises to the reaction onset temperature. The first stage shows a significant exothermic peak, which only lasts 30 minutes. Then, the system temperature decreases and remains consistent with the set value at the second stage.

According to the DSC curve in Fig. 1(a) and Fig. 2(a), the magnesiothermic reduction kinetic parameters without and with NaCl in the system were calculated. Assuming  $\beta$  being the ramp rate, starting temperature is  $T_0$ , and the temperature at the moment  $t$  being  $T = T_0 + \beta t$ , thus,  $dT = \beta dt$ . The reaction kinetics basic formula of the non-isothermal thermal analysis is based as follows [35]:

$$\frac{d\alpha}{dT} = k_0 \frac{f(\alpha)}{\beta} = \frac{A}{\beta} (1 - \alpha)^n \exp(-E / RT) \quad (2)$$

Where  $\alpha$  is conversion rate;  $k_0$  is reaction rate constants;  $A$  is the preexponential factor;  $n$  is reaction order;  $E$  is activation energy;  $R$  is the gas constant,  $8.314 \text{ J}\cdot\text{mol}^{-1}\cdot\text{K}^{-1}$ .

The DSC curve in Fig. 1(a) and Fig. 2(a) integrated to obtain  $H$  (heat of reaction accumulation value) at the corresponding temperature point. The modified heat conversion rate ( $\alpha$ ) can be acquired from  $H$  and  $H_0$  (total heat effect), as shown in Fig. 4.

The kinetic parameters of the reaction were calculated using the Freeman – Carroll method. The Freeman – Carroll method [36] is widely used without any prior knowledge of the reaction order, the apparent activation energy and order of reaction may be calculated from a single experimental curve. Liu [37] pointed out that the Freeman-Carroll method can only be used to determine the activation energy of a reaction accurately and has a significant error in calculating the reaction order. Therefore, only the apparent activation energy of the reaction was discussed here.

$$\frac{\Delta \lg(d\alpha/dT)}{\Delta \lg(1 - \alpha)} = -\frac{E}{19.144} \frac{\Delta(1/T)}{\Delta \lg(1 - \alpha)} + n$$

3

This allows obtaining the activation energy  $E$  and the reaction order  $n$  from the slope and the intercept of a straight line. According to the fitted straight line in Fig. 5, the Freeman – Carroll formula without NaCl in the system can be obtained as:

$$\frac{\Delta \lg(d\alpha/dT)}{\Delta \lg(1 - \alpha)} = -10105.3 \frac{\Delta(1/T)}{\Delta \lg(1 - \alpha)} + 1.2$$

4

The Freeman – Carroll formula with NaCl in the system can be obtained as:

$$\frac{\Delta \lg(d\alpha/dT)}{\Delta \lg(1 - \alpha)} = -9999.7 \frac{\Delta(1/T)}{\Delta \lg(1 - \alpha)} + 3.1$$

5

The Freeman – Carroll formula indicates that the apparent activation energy of the reaction was 193.456 kJ·mol<sup>-1</sup> (without NaCl) and 191.434 kJ·mol<sup>-1</sup> (with NaCl) in the temperature interval 465 – 700°C, respectively. It means that NaCl does not change the apparent activation energy of the reaction, i.e., NaCl is not involved in the reaction. It is known that when the apparent activation energy is between 42 kJ·mol<sup>-1</sup> and 420 kJ·mol<sup>-1</sup>, the limiting link of the reaction is the chemical reaction process[38]. Therefore, the chemical reaction controls the magnesiothermic reduction, and lowering the temperature will reduce the concentration of activated molecules and further decrease the reaction rate. NaCl is lowering the temperature of the system by heat absorption, thereby reducing the rate at which the reaction occurs.

Table 2 showed that the Gibbs free energy change ( $\Delta G$ ) and enthalpy changes ( $\Delta H$ ) of different reactions were calculated by HSC 6.0 software. Obviously, all reactions in Table 2 are negative enthalpies reactions. The  $\Delta G$  of four equations at 450°C – 650°C, 101325 Pa indicate that the first four reactions could be more easily achieved in thermodynamic conditions than reaction (5), and the reaction proceeds more completely at chemical equilibrium.

Table 2  
The  $\Delta H$  and  $\Delta G$  of different reactions (450°C ~ 650°C, 101325 Pa)

Equations	Chemical reaction	$\Delta H(\text{KJ}\cdot\text{mol}^{-1})$	$\Delta G(\text{KJ}\cdot\text{mol}^{-1})$
1	$2\text{Mg}_{(g)} + \text{SiO}_{2(s)} = \text{Si}_{(s)} + 2\text{MgO}_{(s)}$	- (580 ~ 579)	- (396 ~ 345)
2	$4\text{Mg}_{(g)} + \text{SiO}_{2(s)} = \text{Mg}_2\text{Si}_{(s)} + 2\text{MgO}_{(s)}$	- (944 ~ 940)	- (606 ~ 522)
3	$2\text{Mg}_{(g)} + \text{Si}_{(s)} = \text{Mg}_2\text{Si}_{(s)}$	- (366 ~ 360)	- (200 ~ 150)
4	$\text{Mg}_2\text{Si}_{(s)} + \text{SiO}_{2(s)} = 2\text{MgO}_{(s)} + 2\text{Si}_{(s)}$	- (213 ~ 204)	- (192 ~ 190)
5	$\text{SiO}_{2(s)} + 2\text{MgO}_{(s)} = \text{Mg}_2\text{SiO}_{4(s)}$	- (62 ~ 64)	- (58 ~ 62)

Figure 6 presents the XRD patterns of the products obtained by turn-off heating power when the system temperature reaches the exothermic spike (0 h) and different reaction duration under 650°C. As shown in 0 h of Fig. 6(a), the products from MRR contain MgO, Mg<sub>2</sub>Si, Si, and Mg<sub>2</sub>SiO<sub>4</sub> without indication of Mg, which indicates that the reaction between Mg and SiO<sub>2</sub> is rapid and the Mg is consumed entirely. This observation can be confirmed by the DSC curve of the magnesiothermic reduction SiO<sub>2</sub> in Fig. 1(a) since there is no pronounced peak of Mg melting heat absorption observed at 648°C. The disappearance of the Mg phase indicates that reactions (1), (2), and (3) of Table 2 have been completed. The large quantities

of heat released are why the synthesis of  $Mg_2SiO_4$  via Eq. (5), which consumes the residual reactant  $SiO_2$ . These four reactions were completed within 20 minutes (the time used for the system temperature to pass from the reaction start temperature ( $465^\circ C$ ) to  $465^\circ C$  again) shown in Fig. 1(b). The product composition was almost constant with extended durations. XRD patterns at  $650^\circ C$  for 2 h, 4 h and 8 h proved this point.

However, the typical diffraction peaks of Si, MgO, and  $Mg_2Si$  can be detected obviously in Fig. 6(b), which means that adding NaCl into the reactant could inhibit the formation of  $Mg_2SiO_4$  effectively. Thus there is no indication of  $Mg_2SiO_4$  in the mixture. Figures 7(a)–(d) shows the SEM micrograph and constituent elemental distributions inside the particles (obtained at 0 h and washed by glycol). The particles with a diameter of approximately  $25\ \mu m$  and internal porous morphology were observed. Furthermore, the non-homogeneous elemental distributions of O, Mg, and Si over the particles are shown in the EDS mapping images (Figs. 7(b) – 7(d)). Mg elemental content decreases from the outer layer to the inside, i.e., forming a concentration gradient along the radial direction, which is confirmed by EDS analysis in Fig. 7(e). It could be deduced that  $Mg_2Si$  and MgO in a 1 : 2 mole ratio roughly generated within the outer layer of the precursor  $SiO_2$  particle when forming Si and MgO also at a molar ratio 1 : 2 approximately at grain inside. O elemental of grain outer surface more than the scale value is that the small amount Si has been oxidized. What's more, it also suggests the  $Mg_2Si$  and MgO are generated via reaction (2) at the outer layer  $SiO_2$  aggregate. With Mg gas diffusion to the inner reaction interface, the Mg gas concentration decreases, forming Si and MgO via reaction (1) at grain inside the  $SiO_2$  aggregate. The newly generated Si produced near the Mg source will be further converted to form the  $Mg_2Si$ , reaction (3). These three reactions were completed within 30 minutes (the time used for the system temperature to pass from the reaction start temperature ( $475^\circ C$ ) to  $475^\circ C$  again) shown in Fig. 2(b).

With the increase of reaction durations, the content of Si increases while  $Mg_2Si$  decreases, as proved by the increase in the sharp diffraction peaks strength of the phase of Si and decrease of the  $Mg_2Si$  peak strength, as shown in Fig. 6(b). Only MgO and Si diffraction sharp peaks are present in the reaction product without diffraction peaks of  $Mg_2Si$  under 8 h. The conversion rate of  $SiO_2$  to Si with different reaction durations (Table 3) further confirms these results, showing a 58% conversion rate after 0 h, but the value increased to 62% and 75% after 2 h and 4 h, respectively. Note that the conversion rate of  $SiO_2$  is up to 92% when the reaction duration is extended to 8 h at  $650^\circ C$ .

Table 3  
The conversion rate of  $SiO_2$  to Si at 0 h and with different reaction durations under  $650^\circ C$  (with NaCl)

Reaction durations (h)	0	2	4	8
Conversion (%)	58	62	75	92

As shown in Fig. 8, the XRD of three mixtures indicates that synthesized products Si demonstrate different levels of sharp and narrow diffraction peaks without apparent amorphous scattering, indicating a high degree of crystallinity, clearly states that amorphous  $\text{SiO}_2$  transformed into crystalline Si after the MRR. In addition, it demonstrates that the product Si obtained in 0NaCl – 0 h has sharper peaks compared with that of the Si received in 5NaCl – 0 h and 5NaCl – 8 h, confirming larger crystallite sizes. These results are consistent with the general observation in the literature that added NaCl into reactants could inhibit excessive growth of Si crystalline grains by reducing heat accumulated. Furthermore, compared to the full width at half maximum of the XRD peaks of 5NaCl – 0 h with 5NaCl – 8 h, and we can see that the size of the Si crystal grains grows with increasing reaction duration. This observation is further confirmed by the TEM images of the Si display in Figs. 9(g) and 9(h). We also calculated the fine size of Si crystalline grains by Scherrer analysis based on the XRD patterns of Fig. 8. This yielded an average Si crystallite size of 58.201 nm, 24.835 nm, and 41.034 nm, corresponding to 0NaCl – 0 h, 5NaCl – 0 h, and 5NaCl – 8 h, respectively. In brief, the high temperature would lead to excessive growth of the products Si nanoparticles. Meanwhile, Si crystalline grains would also grow to a specific crystal shape due to the diffusion of Si atoms and the migratory movement of grains with reaction duration increases at a higher reaction temperature ( $650^\circ\text{C}$ ).

Figure 9 displays the SEM and TEM images of reactant  $\text{SiO}_2$  and the products Si. It shows that the size of the  $\text{SiO}_2$  particle is  $20\ \mu\text{m}$ , as indicated in Fig. 9(a), and each particle is composed of many primary  $\text{SiO}_2$  nanoparticles (about 25 nm) in Fig. 9(e). As shown in Fig. 9(b), the structure of the obtained product Si changes dramatically compared with that of the precursor  $\text{SiO}_2$ . The smaller nanopores disappear. In contrast, the inter-adhesive macroporous network with a pore diameter ( $\sim 200\ \text{nm}$ ) and a wall thickness ( $\sim 50\ \text{nm}$ ) comes into being, which is further confirmed in Fig. 9(f). The Si particles obtained with NaCl are illustrated in Fig. 9(c), which essentially maintain the morphological structure of the precursor  $\text{SiO}_2$  due to its heat scavenger effect. And the Si nanoparticles with a diameter of about 25 nm show in Fig. 9(g), which is consistent with the result calculated from Scherrer analysis, are loosely interlinked to compose the Si particles around  $12.5\ \mu\text{m}$  (Fig. 9(c)). Compared to the precursor  $\text{SiO}_2$ , micron-sized spherical Si particles exhibit volume shrinkage due to the removal of  $\text{Mg}_2\text{Si}$ ,  $\text{MgO}$ , and  $\text{SiO}_2$ . Figures 9(d) and (h) show that the structure of the Si also maintained the spherical morphological of the precursor  $\text{SiO}_2$  after extending the duration to 8 h at  $650^\circ\text{C}$ . However, the Si particles diameter increases to around  $18\ \mu\text{m}$ , and the primary Si nanoparticles diameter also increases to about 40 nm. It clearly illustrates that crystal grains grow in a specific crystal shape with increasing reaction duration, consistent with the results obtained in Fig. 8.

## 4 Conclusions

Magnesiothermic reduction slowly occurs at the initial stage ( $465^\circ\text{C} - 535^\circ\text{C}$ ), and the Mg pressure increases with the temperature rise. The reaction is drastic once the Mg vapor pressure is sufficient to diffuse into the  $\text{SiO}_2$  particles (at  $535^\circ\text{C}$ ). The Mg vapor diffusion process will lead to a concentration gradient along the radial direction in  $\text{SiO}_2$  aggregate. It caused that  $\text{Mg}_2\text{Si}$  and  $\text{MgO}$  are generated at the

outer layer while Si and MgO formed at grain inside the SiO<sub>2</sub> aggregate. What's more, The newly generated Si produced near the Mg source will be further also converted to form Mg<sub>2</sub>Si. The heat released from the reaction will lead to a transient high temperature and the formation of the byproduct Mg<sub>2</sub>SiO<sub>4</sub>, which consumes SiO<sub>2</sub> and MgO. All reactions without NaCl are completed within approximately 20 minutes after the system temperature reaches onset temperature.

As a heat scavenger, NaCl does not affect the apparent activation energy of the reaction, and it affects the reaction mechanism by lowering the temperature of the system. Mg<sub>2</sub>SiO<sub>4</sub> is not generation in system, but the reaction (1), (2), and (3) occurs in the same order as before the addition of NaCl. These three reactions are completed within 30 minutes after the system temperature reaches onset temperature. And the diameter of the initial prepared Si nanoparticles is about  $D_{(0.5)} = 25$  nm. What's more, the formed Mg<sub>2</sub>Si phase could reduce the residue SiO<sub>2</sub> in the next 8 h, which leads to the highest conversion ratio (92%) of SiO<sub>2</sub>, and the diameter of Si nanoparticles obtained increases to  $D_{(0.5)} = 40$  nm.

## 5 Declarations

### Acknowledgments

I would like to express my sincere gratitude to my tutor and senior students for their guidance and help in completing this work. Also, I especially thank the Analytical and Testing Center, Northeastern University (China), for the instrumental or data analysis.

### Funding

Not applicable

### Conflicts of interest/Competing interests

Have no known competing financial interests or personal relationships that could have appeared to influence the work reported in this paper.

### Availability of data and material

Not applicable

### Code availability

Not applicable

### Author contributions

Material preparation, data collection, and analysis were performed by Boxia Zhang, Fei Wang, Jianshe Chen, Binchuan Li, Kuiren Liu, Qing Han. The first draft of the manuscript was written by Boxia Zhang and

all authors commented on previous versions of the manuscript. All authors read and approved the final manuscript.

### **Consent to participate**

All authors happily agree to participate in this research study.

### **Consent for Publication**

All authors permit the permission to the journal to publish this research study.

### **Ethics approval**

Not applicable

## **6 References**

1. Park J, Kim GP, Nam I, Park S, Yi J (2013) One-pot synthesis of silicon nanoparticles trapped in ordered mesoporous carbon for use as an anode material in lithium-ion batteries. *Nanotechnology* 24(2):025602
2. Sun LM, Wang XH, Susantyoko RA, Zhang Q (2014) Copper-silicon core-shell nanotube arrays for free-standing lithium-ion battery anodes. *J Mater Chem A* 2(37): 15294
3. Chen H, Wang S, Liu X, Hou X, Chen F, Pan H, Qin H, Lam KH, Xia Y, Zhou G (2018) Double-coated si-based composite composed with carbon layer and graphene sheets with void spaces for lithium-ion batteries. *Electrochim Acta* 288: 134–143
4. Zuo X, Zhu J, Buschbaum PM, Cheng Y (2017) Silicon based lithium-ion battery anodes: a chronicle perspective review. *Nano Energy* 31:113–143
5. Yao KP, Okasinski JS, Kalaga K, Almer JD, Abraham DP (2019) Operando quantification of (De)lithiation behavior of silicon-graphite blended electrodes for lithium-ion batteries. *Adv Energy Mater* 9(8):1803380
6. Teki R, Datta MK, Krishnan R, Parker TC, Lu TM, Kumta PN, Koratkar N (2009) Nanostructured silicon anodes for lithium ion rechargeable batteries. *Small* 5(20):2236–2242
7. Iqbal A, Chen L, Chen Y, Gao YX, Chen F, Li DC (2018) Lithium-ion full cell with high energy density using nickel-rich  $\text{LiNi}_8\text{Co}_{0.1}\text{Mn}_{0.1}\text{O}_2$  cathode and SiO-C composite anode. *Int J Miner Metall Mater* 26(3):386–386
8. Xie Y, He CJ, Zhang J, Hou YL, Meng WJ, Zhao DL (2021) Nitrogen-doped carbon caging silicon nanoparticles for high performance lithium-ion battery anodes. *J Alloy Compd* 860:158487
9. Bhandavat R, Singh G (2013) Stable and efficient li-ion battery anodes prepared from polymer-derived silicon oxycarbide-carbon nanotube shell/core composites. *J Phys Chem C* 117(23):11899–11905

10. Gao XF, Wang FF, Gollon S, Yuan C (2019) Micro silicon-graphene-carbon nanotube anode for full cell lithium-ion battery. *J Electrochem Energy Convers Storage* 16(1):011009
11. Park MH, Kim MG, Joo J, Kim K, Kim J, Ahn S, Cui Y, Cho J (2009) Silicon nanotube battery anodes. *Nano Lett* 9(11):3844–3847
12. Nguyen HT, Yao F, Zamfir MR, Biswas C, So KP, Lee YH, Kim SM, Cha SN, Kim JM, Privat D (2011) Highly interconnected si nanowires for improved stability li-ion battery anodes. *Adv Energy Mater* 1(6):1154–1161
13. Kim H, Han B, Choo J, Cho J (2008) Three-dimensional porous silicon particles for use in high-performance lithium secondary batteries. *Angew Chem Int Edit* 47(52):10151–10154
14. Yao Y, McDowell MT, Ryu I, Wu H, Liu N, Hu LB, Nix WD, Cui Y (2011) Interconnected silicon hollow nanospheres for lithium-ion battery anodes with long cycle life. *Nano Lett* 11(7):2949–2954
15. Wang XL, Han WQ (2010) Graphene enhances li storage capacity of porous single-crystalline silicon nanowires. *ACS Appl Mater Interfaces* 2(12):3709–3713
16. Fuchsbichler B, Stangl C, Kren H, Uhlig F, Koller S (2011) High capacity graphite-silicon composite anode material for lithium-ion batteries. *J Power Sources* 196(5): 2889–2892
17. An WL, Xiang B, Fu JJ, Mei SX, Guo SG, Huo KF, Zhang XM, Gao B, Chu PK (2019) Three-dimensional carbon-coating silicon nanoparticles welded on carbon nanotubes composites for high-stability lithium-ion battery anodes. *Appl Surf Sci* 479:896–902
18. Wu LL, Zhou HC, Yang J, Zhou XY, Ren YP, Nie Y, Chen S (2017) Carbon coated mesoporous si anode prepared by a partial magnesiothermic reduction for lithium-ion batteries. *J Alloy Compd* 716:204–209
19. Sethuraman VA, Kowolik K, Srinivasan V (2011) Increased cycling efficiency and rate capability of copper-coated silicon anodes in lithium-ion batteries. *J Power Sources* 196(1):393–398
20. Liu N, Wu H, McDowell MT, Yao Y, Wang CM, Cui Y (2012) A yolk-shell design for stabilized and scalable li-ion battery alloy anodes. *Nano Lett* 12(6):3315–3321
21. Priolo F, Gregorkiewicz T, Galli M, Krauss TF (2014) Silicon nanostructures for photonics and photovoltaics. *Nat Nanotechnol* 9(1):19–32
22. Dai F, Zai JT, Yi R, Gordin ML, Sohn H, Chen SR, Wang DH (2014) Bottom-up synthesis of high surface area mesoporous crystalline silicon and evaluation of its hydrogen evolution performance. *Nat Commun* 5:3605
23. Bux SK, Blair RG, Gogna PK, Lee H, Chen G, Dresselhaus MS, Kaner RB, Fleurial JP (2009) Nanostructured bulk silicon as an effective thermoelectric material. *Adv Funct Mater* 19(15) :2445–2452
24. Bao Z, Weatherspoon MR, Shian S, Cai Y, Graham PD, Allan SM, Ahmad G, Dickerson MB, Church BC, Kang ZT, Abernathy III HW, Summers CJ, Liu M, and Sandhage KH (2007) Chemical reduction of three-dimensional silica micro-assemblies into microporous silicon replicas. *Nature* 446(7132):172–175

25. Xiang B, An WL, Fu JJ, Mei SX, Guo SG, Zhang XM, Gao B, Chu PK (2020) Graphene-encapsulated blackberry-like porous silicon nanospheres prepared by modest magnesiothermic reduction for high-performance lithium-ion battery anode. *Rare Metals* 40(2):383–392
26. Wu JX, Qin XY, Zhang HR, He YB, Li BH, Ke L, Lv W, Du HD, Yang QH, Kang FY (2015) Multilayered silicon embedded porous carbon/graphene hybrid film as a high performance anode. *Carbon* 84:434–443
27. Darghouth A, Aouida S, Bessais B (2021) High Purity Porous Silicon Powder Synthesis by Magnesiothermic Reduction of Tunisian Silica Sand. *Silicon* 13(3):667–676
28. Liu XH, Zhong L, Huang S, Mao SX, Zhu T, Huang JY (2012) Size-dependent fracture of silicon nanoparticles during lithiation. *Acs Nano* 6(2):1522–1531
29. Won CW, Nersisyan HH, Won HI (2011) Solar-grade silicon powder prepared by combining combustion synthesis with hydrometallurgy. *Sol Energy Mater Sol Cells* 95(2):745–750
30. Shi L, Wang WK, Wang AB, Yuan KG, Yang YS (2016) Understanding the impact mechanism of the thermal effect on the porous silicon anode material preparation via magnesiothermic reduction. *J Alloy Compd* 661:27–37
31. Meekins BH, Lin YC, Manser JS, Manukyan K, Mukasyan AS, Kamat PV, McGinn PJ (2013) Photoactive porous silicon nanopowder. *ACS Appl Mater Interfaces* 5(8):2943–2951
32. Yang ZX, Du Y, Hou GL, Ouyang YG, Ding F, Yuan FL (2020) Nanoporous silicon spheres preparation via a controllable magnesiothermic reduction as anode for li-ion batteries. *Electrochim Acta* 329:135141
33. Xie J, Wang GQ, Huo Y, Zhang SC, Cao GS, Zhao XB (2014) Nanostructured silicon spheres prepared by a controllable magnesiothermic reduction as anode for lithium ion batteries. *Electrochim Acta* 135:94–100
34. Brindley GW, Hayami R (1965) Kinetics, and mechanism of formation of forsterite ( $Mg_2SiO_4$ ) by solid state reaction of  $MgO$  and  $SiO_2$ . *Philos Mag* 12(117):505–514
35. Li YZ (1987) Thermo-analysis. Tsinghua University Press, Beijing
36. Freeman BE, Carroll B (1957) The application of thermoanalytical techniques to reaction kinetics: The thermogravimetric evaluation of the kinetics of the decomposition of calcium oxalate monohydrate. *The Journal of Physical Chemistry* 62:394–397
37. Liu NA, Fan WC (2000) Critical consideration on the Freeman and Carroll method for evaluating global mass loss kinetics of polymer thermal degradation. *Thermochimica Acta* 351(1):183–183
38. Tian YW, Zhai XJ, Liu KR (2011) A Concise Course of Metallurgical Physical Chemistry. Chemical Press, Beijing

## Figures

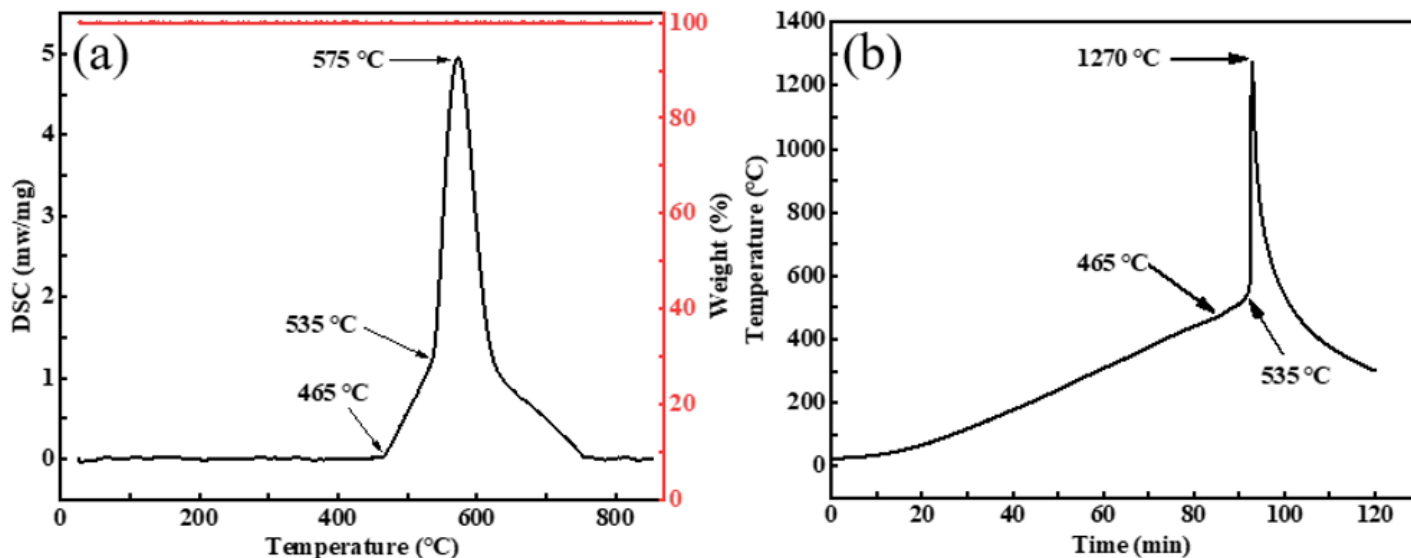


Figure 1

TG-DSC diagram (a) of the magnesiothermic reduction  $\text{SiO}_2$  with  $5\text{ }^\circ\text{C}\cdot\text{min}^{-1}$  under argon atmosphere from  $20\text{ }^\circ\text{C}$  to  $800\text{ }^\circ\text{C}$  and the temperature profile (b) of the magnesiothermic reduction  $\text{SiO}_2$ .

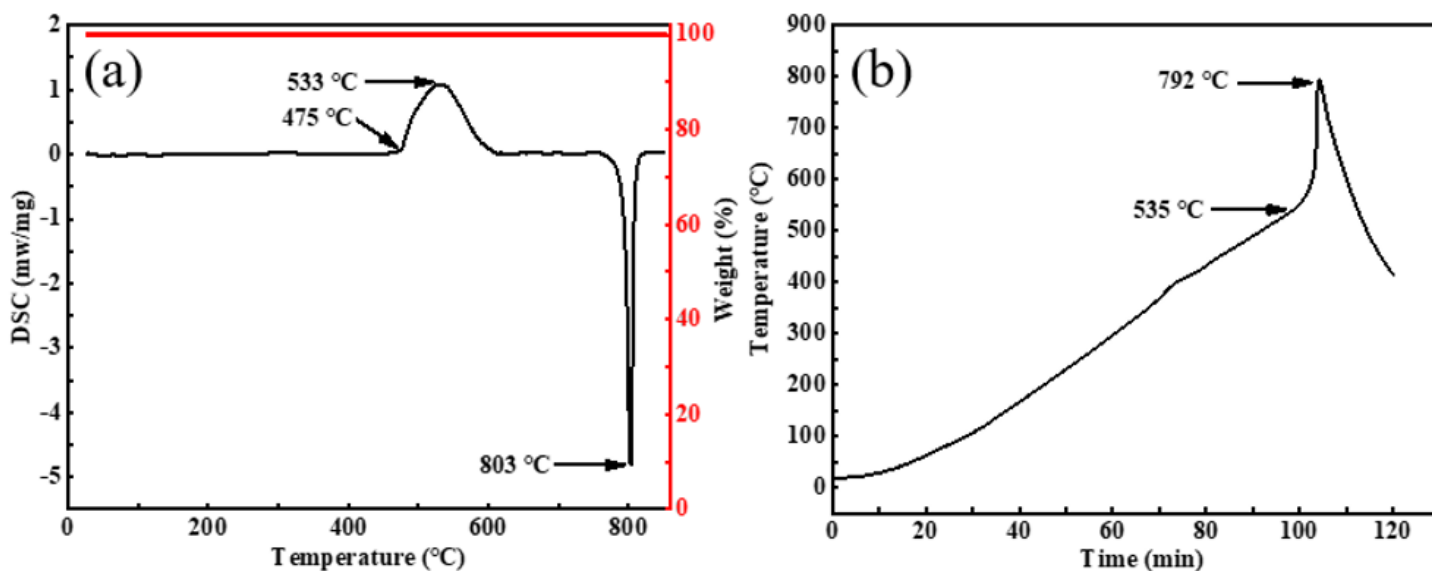


Figure 2

TG-DSC diagram (a) of the magnesiothermic reduction  $\text{SiO}_2$  with  $5\text{ }^\circ\text{C}\cdot\text{min}^{-1}$  under argon atmosphere from  $20\text{ }^\circ\text{C}$  to  $800\text{ }^\circ\text{C}$  (with NaCl); The temperature profile (b) of the magnesiothermic reduction  $\text{SiO}_2$  (with NaCl).

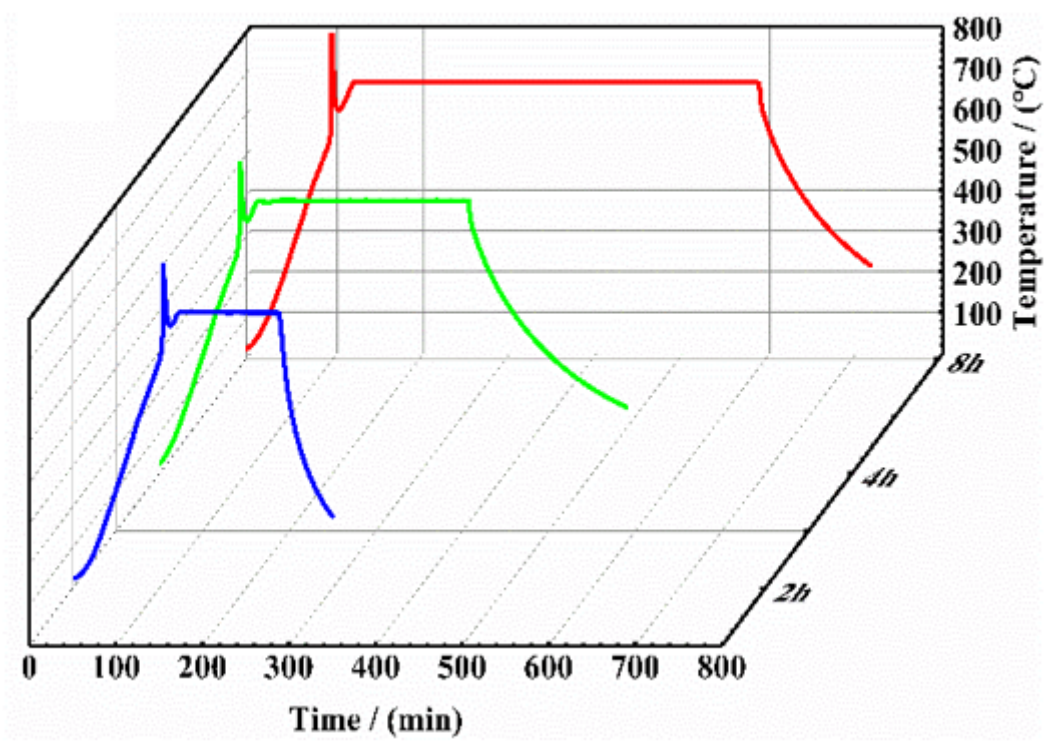


Figure 3

The temperature profiles of the magnesiothermic reduction  $\text{SiO}_2$  with different reaction duration at 650 °C.

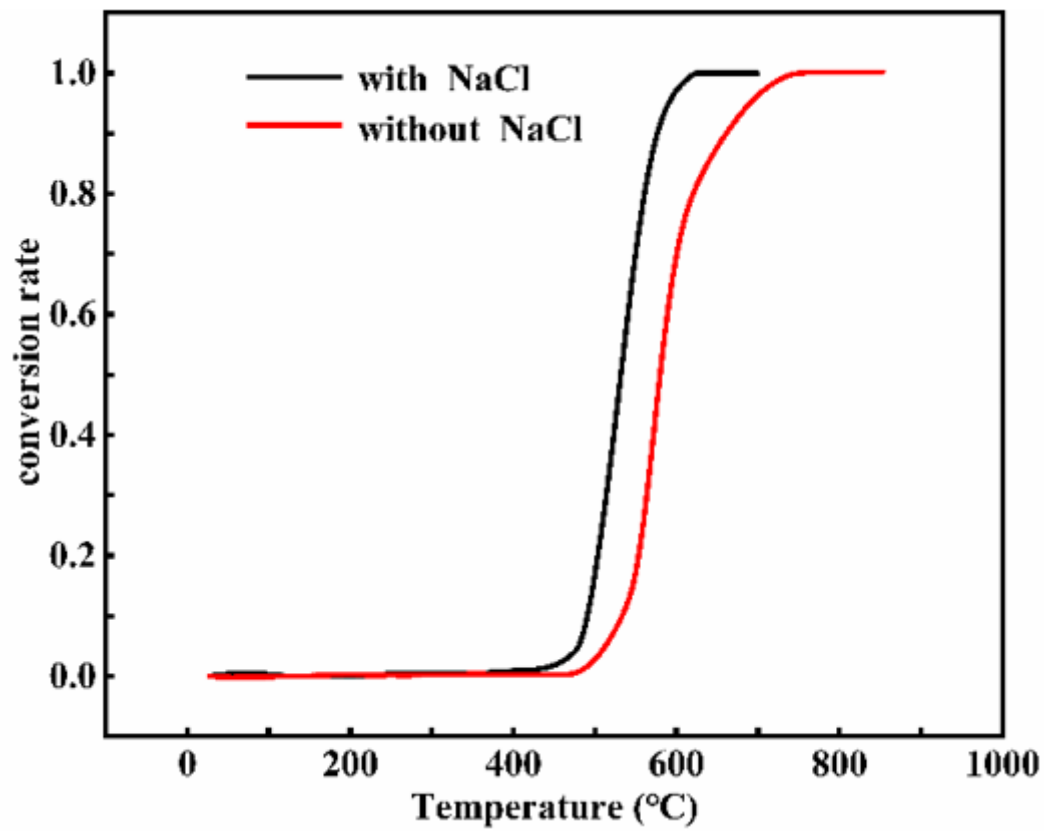


Figure 4

Modified heat conversion rate (a) curve of the magnesiothermic reduction

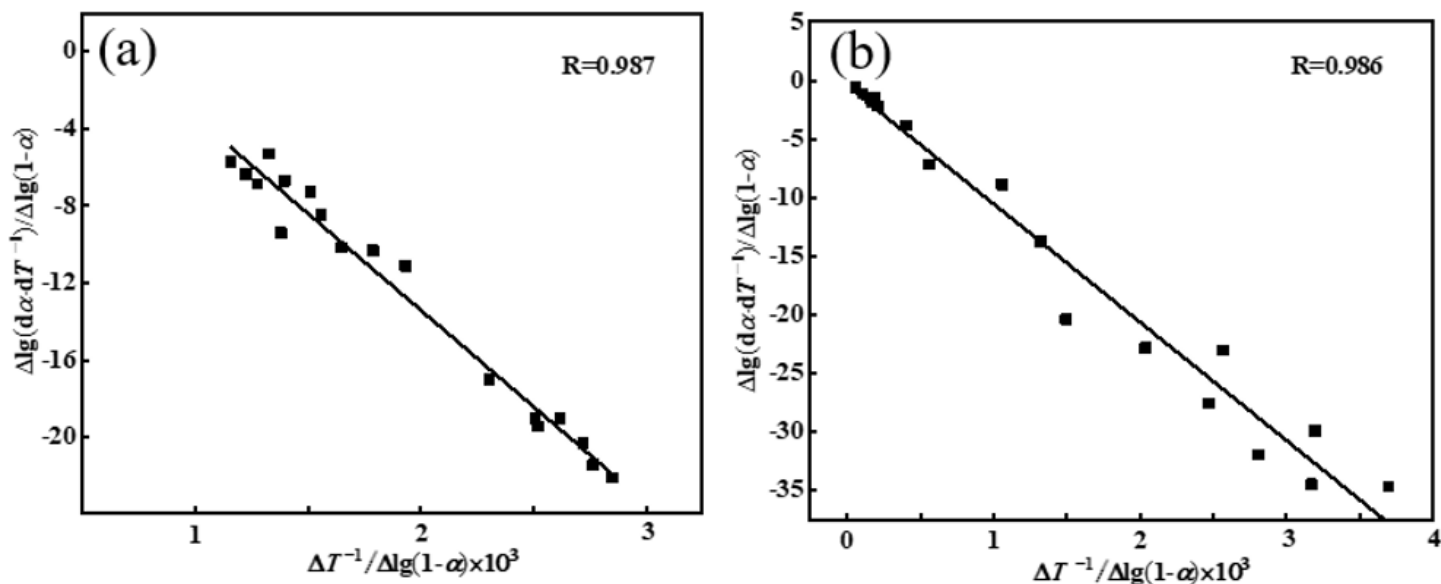


Figure 5

The Freeman-Carroll curve of the magnesiothermic reduction  $\text{SiO}_2$  at exothermic peak: (a) without NaCl; (b) with NaCl

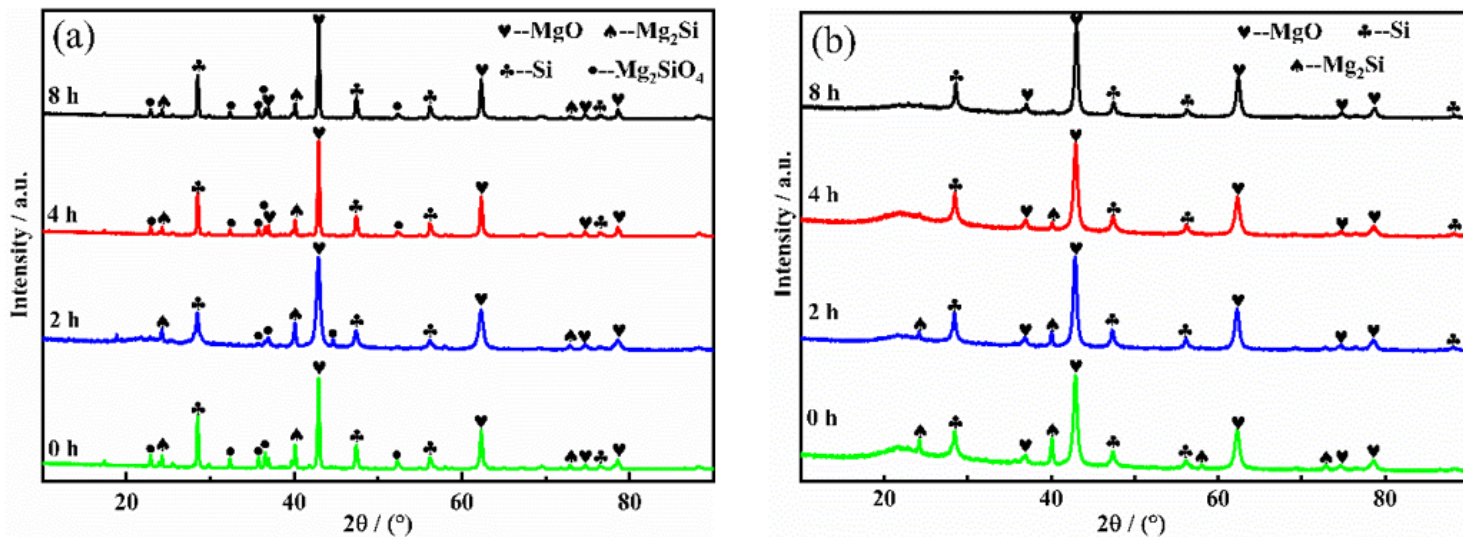


Figure 6

XRD diffraction patterns of the products with 0 h and different reaction durations at  $650^\circ\text{C}$ : (a) without NaCl; (b) with NaCl (products were washed with ethylene glycol).

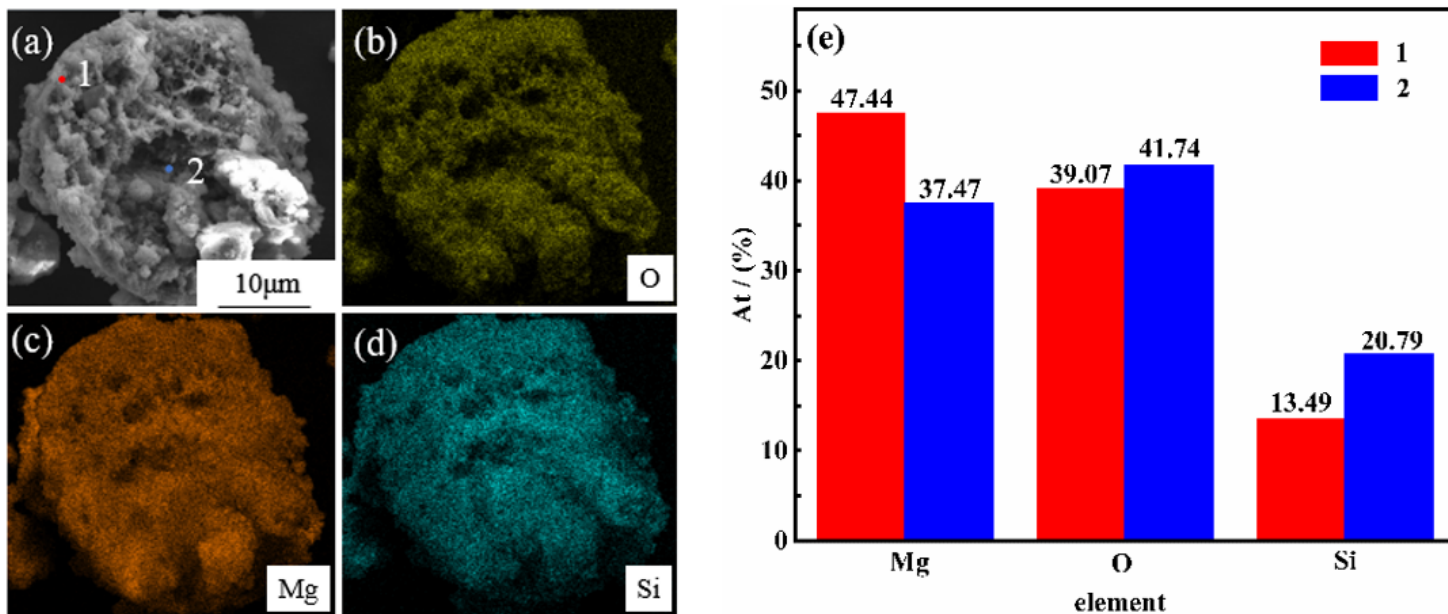


Figure 7

SEM image (a) of the product particle internal obtained at 0 h and washed by glycol; EDS elemental mapping images of (b) O, (c) Mg, and (d) Si for (a); EDS elemental analysis (e) of Mg, O, and Si for 1 and 2 in (a).

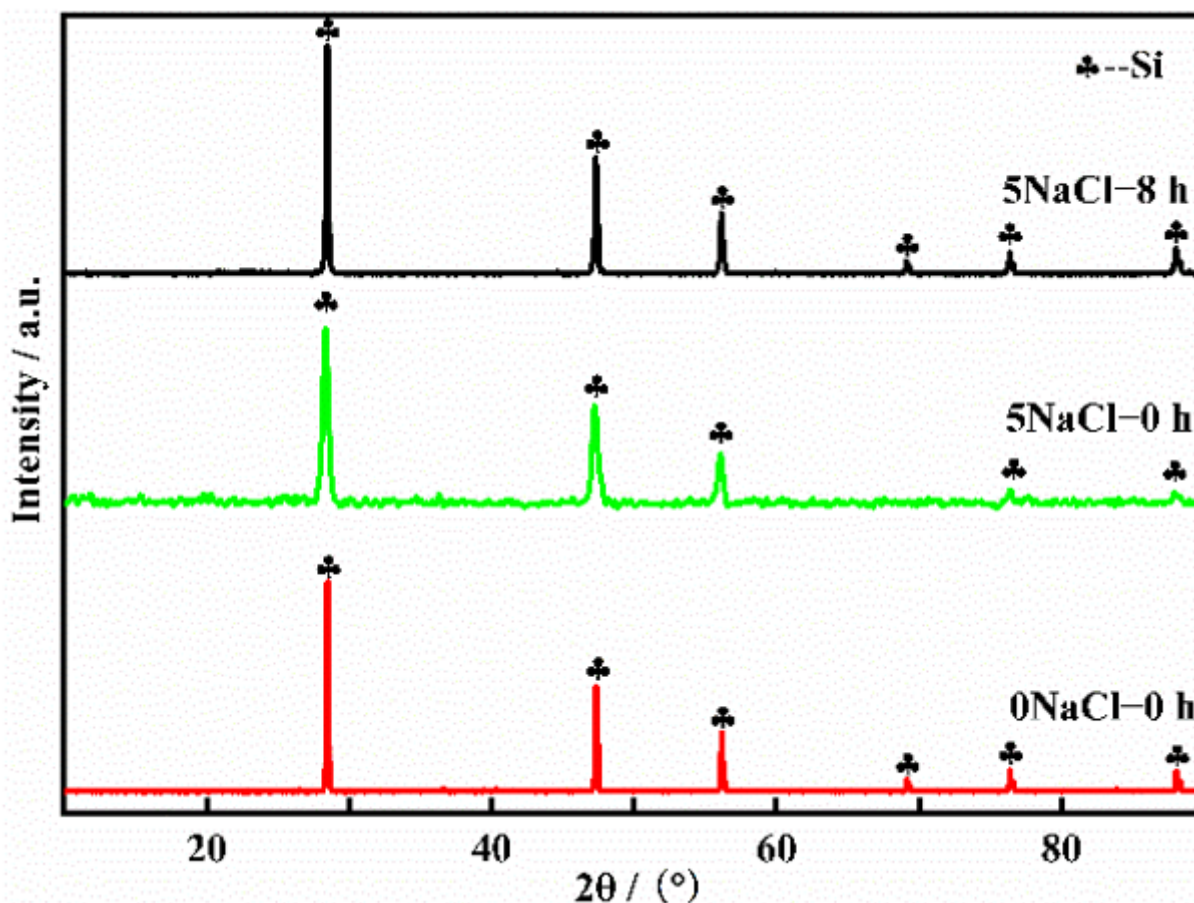
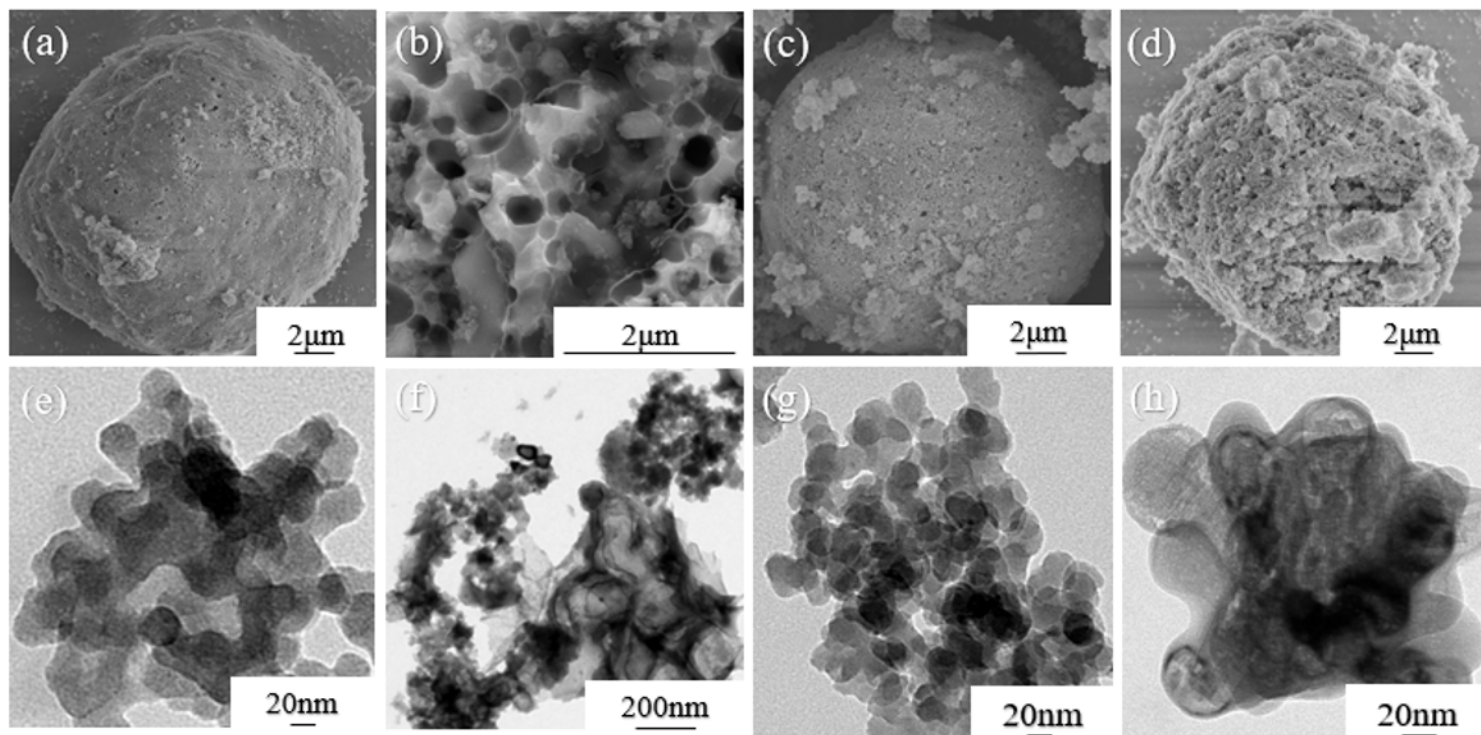


Figure 8

XRD diffraction patterns of the products Si with different reaction duration. (0 h and without NaCl in reactants, denoted as 0NaCl-0 h; 0 h and with NaCl, denoted as 5NaCl-0 h; 8 h at 650 °C and with NaCl, denoted as 5NaCl-8 h)



**Figure 9**

SEM and TEM images of samples. (a and e) reactant SiO<sub>2</sub>; products Si: (b and f) 0NaCl-0 h; (c and g) 5NaCl-0 h; (d and h) 5NaCl-8 h.